Journal of Catalysis **203,** 104–121 (2001)
doi:10.1006/jcat.2001.3312, available online at http://www.idealibrary.com on IDEAL®

The Origin of the Ligand Effect in Metal Oxide Catalysts: Novel Fixed-Bed *in Situ* Infrared and Kinetic Studies during Methanol Oxidation

Loyd J. Burcham,[1] Mohit Badlani, and Israel E. Wachs[2]

Zettlemoyer Center for Surface Studies and Department of Chemical Engineering, Lehigh University, Bethlehem, Pennsylvania 18015

Received December 28, 2000; revised May 7, 2001; accepted May 13, 2001

Supported and bulk metal oxide catalysts generally exhibit a "ligand effect" in the selective oxidation of methanol to formaldehyde. This phenomenon is identified by orders of magnitude variations in the turnover frequency (TOF; TOF = activity per active surface site) of the same active metal oxide metal atom, for example, V or Mo active sites, as changes are made in the choice of support cation or bulk mixed metal oxide co-cation. The mechanistic origin of this ligand effect has been investigated in the present study using a novel *in situ* IR cell designed to operate as a fixed-bed catalytic reactor with coupling to an online gas chromatograph for analysis of gas-phase product distributions. The active site determinations required for calculation of TOFs were performed using methanol chemisorption and IR spectroscopy. Moreover, under actual methanol oxidation reaction conditions, quantification of the adsorbed, steady-state concentrations of methoxylated surface intermediates by *in situ* IR spectroscopy allowed for decoupling of the reaction mechanism to yield individual estimates of the adsorption and surface reaction kinetic parameters. Comparisons of the relative values of the adsorption equilibrium constant, K_{ads}, and the kinetic rate constant for the surface decomposition step, k_{rds}, indicate that the TOF clearly correlates with the rate constant for the surface decomposition step. For example, supported vanadia catalysts exhibit a 12-fold increase in the surface decomposition rate constant, k_{rds}, for vanadia supported on silica, alumina, titania, and ceria supports. Conversely, the adsorption constant, K_{ads}, is relatively invariant for vanadia supported on silica, alumina, and titania, decreasing in value by about half only for the vanadia/ceria catalyst. It also appears that the origin of the ligand effect is fundamentally related to the electronegativity of the ligand cation, the more electropositive ligands (titania and ceria support cations) always having higher TOFs than the more electronegative ligands (alumina and silica support cations). Most likely, the ligand cation electronegativity affects the magnitude of the rate-determining surface reaction step, k_{rds}, via its influence on the ability of the active metal cation to decompose the adsorbed methoxylated surface intermediates by hydride abstraction of methyl hydrogen.

Key Words: **methanol oxidation; metal oxides; supported metal oxide catalysts; turnover frequencies; *in situ* infrared spectroscopy; methanol chemisorption.**

1. INTRODUCTION

The application of *in situ* techniques for elucidating fundamental structure–reactivity relationships in heterogeneous catalysis is currently a research topic of great interest (1). One important reaction that has been recently studied is the selective oxidation of methanol to formaldehyde, which is commercially used for the production of phenolic resins (2, 3). Typical industrial catalysts consist of unsupported $Fe_2(MoO_4)_3$–MoO_3 mixtures or silver (2, 3), but high activities and selectivities for this reaction have also been well documented at low conversions in supported metal oxide catalysts, in which the active metal oxide is molecularly dispersed as a two-dimensional metal oxide overlayer on a high surface area support oxide (3, 4). In particular, catalysts with vanadia and molybdena supported on alumina and titania (and less frequently on ceria, zirconia, silica, and niobia) are among the most frequently studied of this type of catalyst (3–17). These supported metal oxide systems are also especially well suited to serve as model catalysts because the supported metal oxide active phase can be readily characterized with *in situ* spectroscopic methods and permits calculations of intrinsic turnover frequency (TOF; TOF = molecules converted per second per *active surface metal oxide site*).

Much of the recent effort with *in situ* spectroscopic techniques centers on determining the origin of the "support effect" observed in supported metal oxide systems. Using fixed-bed activity data, Wachs and co-workers (10, 11) and Niwa and co-workers (15–17) have revealed an order of magnitude difference in TOF over monolayer-supported molybdena catalysts, the more electropositive supports providing the greater activity: $ZrO_2 \sim TiO_2 \gg Nb_2O_5 > Al_2O_3 > SiO_2$(10); $ZrO_2 > TiO_2 > Al_2O_3$(17); and $SnO_2 > Fe_2O_3 \sim ZrO_2 > TiO_2 > Al_2O_3$(15). The

[1] Present address: Congoleum Corporation, P.O. Box 3127, Mercerville, NJ 08619.

[2] To whom correspondence should be addressed.

0021-9517/01 $35.00

support effect in supported vanadia catalysts is even greater than that of supported Mo-based catalysts, spanning 3 orders of magnitude (7–9). As with supported molybdena catalysts, the more electropositive support cations in supported vanadia catalysts yield the greatest TOFs to formaldehyde. Under 6% methanol in O_2/He, the TOFs for supported vanadia catalysts at monolayer coverages were found to be highest for vanadia on ceria ($1.0 \times 10^{+0}$ s^{-1}), followed by V_2O_5/ZrO_2 (1.7×10^{-1} s^{-1}) and V_2O_5/TiO_2 (1.1×10^{-1} s^{-1}), and was much lower for V_2O_5/Al_2O_3 (6.8×10^{-3} s^{-1}) and V_2O_5/SiO_2 (2.0×10^{-3} s^{-1}) (9). A similar ligand effect was also recently observed in bulk molybdate catalysts, in which the TOFs were calculated using active surface site densities measured from methanol chemisorption experiments (18).

Explanations for this support effect have included empirical correlations of the TOF to the support cation electronegativity (9), H_2 temperature-programmed reduction peak temperatures (7, 10, 19), and the relative amounts of polyvanadate clusters as measured by UV-vis diffuse reflectance spectroscopy ligand–metal charge transfer edge energies (20). However, determination of its more fundamental mechanistic origin requires that structure–reactivity relationships be developed for the individual reaction steps (adsorption, surface reaction, and desorption) involved in the overall methanol oxidation reaction. Preliminary studies on the effect of the oxide support on the reaction mechanism have been reported for supported vanadia catalysts using a combined infrared (IR) spectroscopy/mass spectrometry method (21). This previous study demonstrated that the mechanistic parameters associated with adsorption and surface reaction during steady-state methanol oxidation over supported vanadia catalysts can be separately estimated by directly quantifying the steady-state concentrations of the adsorbed methoxy intermediates ($-OCH_3$) present on the catalyst surface during reaction. In the supported vanadia catalysts, the equilibrium adsorption constant, K_{ads}, for methanol dissociative chemisorption to surface methoxy species was found to vary by a factor of ~6 as the specific oxide support was changed. However, the kinetic rate constant for the rate-determining surface decomposition of surface methoxy species to gas-phase formaldehyde, k_{rds}, varied by ~22 times for vanadia on the different oxide supports and indicated that the decomposition step was primarily responsible for the observed support effect in this series of catalysts.

Mass transfer limitations, however, were quite large in the traditional IR flow cell used in the previous study ($E_{app} \sim 10$ kcal/mol instead of ~20 kcal/mol typically obtained in fixed-bed experiments) and required modeling of the IR cell as a single-pellet reactor under diffusion control. Also, the use of a mass spectrometer for gas-phase product detection proved very inaccurate due, partly, to the lack of product separation. In fact, consistent results were obtained in the previous study only by using fixed-bed kinetic data for the final calculations and adjusting their values via the IR cell reactor model to produce estimates of the desired individual reaction step parameters. To improve on these data, a reexamination of the mechanistic origin of the ligand effect in metal oxide catalysts has been undertaken in the present study with an improved and novel experimental design based on the experience obtained from the preliminary study.

A redesign of the IR flow cell was required to mitigate the mass transfer limitations present in the previous study. Infrared flow cell designs have appeared in several forms in the recent literature (22–41) and, as shown in Fig. 1, can be classified according to the gas-flow regime present in the catalyst bed. Traditional transmission IR cells suspend compressed, self-supporting catalyst wafers in a stream of flowing reactant gas in a position normal to both the gas-flow direction and the IR beam path. Although easy to construct, such designs suffer from bypassing and recirculation of the reactant and product gases that create stagnant films around the surfaces of the catalyst wafer and force the flow inside the catalyst to be diffusive rather than convective (21). An improvement has been the elimination of dead volume in the cell by proper design of the gas-flow path (21, 23), which removes the recirculation and bypass issues and permits reasonable assumptions regarding the gas concentrations at the wafer surfaces. The flow inside the catalyst wafer remains largely diffusive in such improved traditional cells, but models of the diffusive flow can be made to estimate the kinetic behavior of the cell. Such an approach was used in the preliminary study discussed previously concerning the origin of the support effect in supported vanadia catalysts (21) and has also been used by Topsoe (23) to study the selective catalytic reduction of NO_x by NH_3.

Another approach that has gained favor in recent years is the placement of the self-supporting catalyst wafer normal to the IR beam path, but *parallel* to the gas-flow direction (25, 26, 28, 30, 32, 33, 36). These more complicated cell designs eliminate the wakes and eddies created by flow normal to the wafer surface, enabling a more detailed modeling of the fluid flow. However, proper analysis requires solving the partial differential equations (Navier–Stokes equations) describing the two- and three-dimensional fluid dynamics at the laminar boundary layers present on the surfaces. Such an analysis was performed by Saladin *et al.* (30) but has otherwise been absent from studies using this type of cell design. The work of Kaul and Wolf (25, 26) has extended the application of such cell designs to include "selected-area" spectroscopy that uses a rotating mask to isolate specific portions of the wafer for localized analysis. Unfortunately, catalysis in this cell design again occurs via diffusion of gas into and out of the wafer and requires additional modeling for kinetic analyses; the need for effective

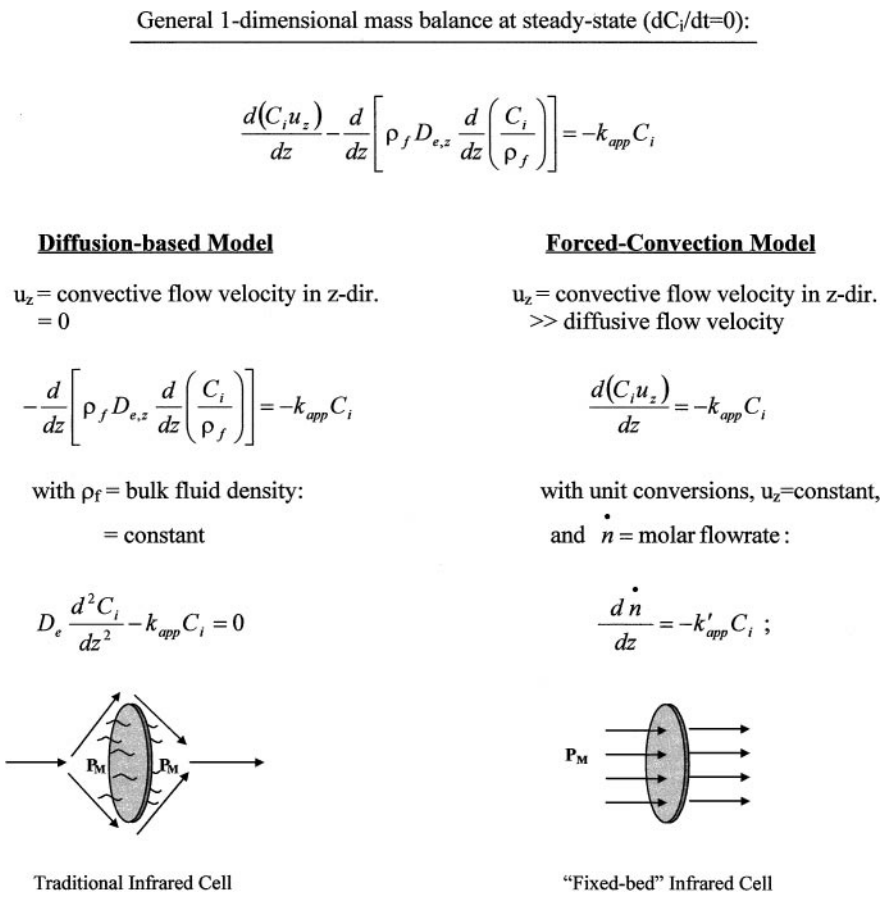

FIG. 1. Flow regimes applicable to *in situ* IR cells during steady-state methanol oxidation.

diffusion constants in all such diffusion-based flow regimes is the largest source of uncertainty.

A more ideal IR flow cell should be configured to operate in a fixed-bed flow regime, in which forced convective gas flow through the catalyst bed eliminates the need for diffusion coefficients and complex fluid dynamics models (see Fig. 1). Cell designs based on diffuse reflectance (DRIFTS) (24, 27, 31) and attenuated total reflection (including fiber optics) (39–41) use powdered catalyst beds as samples, not compressed wafers, and have been reported to have reasonable performance as fixed-bed chemical reactors. However, optical requirements for these techniques often demand large amounts of catalyst that hinder the ability to achieve differential conversions at normal reaction temperatures; many designs contain significant dead volumes, and quantitative analysis is considerably less straightforward for reflection methods than for transmission (which follows Beer's Law). The development of a fixed-bed transmission IR cell would circumvent many of the previously described difficulties, but such designs have been unavailable due to the inability of thin, IR transparent wafers to withstand the pressure drops induced by forced convective flow through them. A notable exception is a design presented by Vannice *et al.* (29) that pressed high surface area catalysts into rings that were sealed into the flow path of an IR cell. However, this cell is limited to materials possessing relatively high mechanical strengths as self-supporting wafers (e.g., alumina-based systems) and has not found widespread use with more fragile materials.

In the present study, a novel fixed-bed transmission IR cell has been developed to investigate the mechanistic origin of the ligand effect in metal oxide catalysts during methanol oxidation. As described in Section 2, the key feature of this cell is the use of thin disks of perforated stainless steel as sample holders into which catalyst powders are pressed. Such a design permits combined IR and kinetic analyses on a great variety of materials because the catalysts no longer need to be pressed into fragile self-supporting wafers and can be positively sealed into the flow path of the cell. Several additional improvements have also been made to the experimental design, relative to the system previously used (21). In particular, a gas chromatograph (GC) has replaced the mass spectrometer for more accurate product analysis. Monolayer coverages were always used for the supported catalysts presently studied because they minimize the amount of exposed adsorption sites on the bare support, which produce stable spectator surface methoxy species rather than reactive intermediates. Finally,

active site densities obtained in recent methanol chemisorption studies (18) have provided an alternative method for calculating TOFs in supported metal oxides that is also applicable to bulk oxides. The implications of using such methanol chemisorption site densities instead of total active metal atoms will be discussed with the kinetic results in later sections.

2. EXPERIMENTAL

2.1. Catalyst Preparation

The supported metal oxide catalysts used in this study were prepared by the incipient wetness impregnation method. This technique is described in detail elsewhere (4, 7–11), so only a brief summary is provided here. The oxide supports (γ-Al_2O_3 with 250 m^2/g from Engelhard or 180 m^2/g from Harshaw, P-25 TiO_2 with 55 m^2/g from Degussa, CeO_2 with 36 m^2/g from Engelhard, and Cabosil EH-5 SiO_2 with 320 m^2/g from Cabot) were first calcined to 723–773 K and then cooled to room temperature. The supports were then impregnated with aqueous solutions of ammonium heptamolybdate, chromium nitrate, or 60–70 wt% perrhenic acid. The moisture-sensitive vanadia precursor, vanadium triisopropoxide, was mixed with methanol to achieve incipient wetness under a nitrogen atmosphere inside a glove box. After thorough mixing, the samples were dried at room temperature in air (in a glove box for vanadia samples) for 16 h, followed by heating to 393 K (under flowing nitrogen for vanadia samples) for 12 h. Finally, the samples were calcined to 723 K (TiO_2, CeO_2, and SiO_2 samples) and 773 K (Al_2O_3 samples) in pure oxygen for 4 h.

All supported metal oxide catalysts correspond to monolayer coverages, except that the relatively inert silica surface and the volatilization of surface rhenia dimers prevents attainment of complete monolayers in these systems (42). Instead, these systems contain the highest loading possible of deposited surface metal oxide that does not form bulk oxide microcrystallites (silica-supported systems) or volatilize (supported rhenia catalysts). Pure bulk ferric molybdate was prepared using a coprecipitation technique that is described in detail elsewhere (43). Phase purities were determined by X-ray diffraction and Raman spectroscopy (see (44) for experimental details), and surface areas were determined with BET instrumentation (Quantachrome Corp., Quantasorb Model OS-9).

2.2. In Situ IR Spectroscopy

The *in situ* IR experiments were performed with a Bio-Rad FTS-40A FTIR Spectrometer equipped with a DTGS detector. The IR spectra were recorded at a resolution of $\sim$2 cm^{-1} using 250 signal-averaged scans and, after acquisition, were smoothed using the Savitsky–Golay method when necessary. The IR was operated in transmission mode

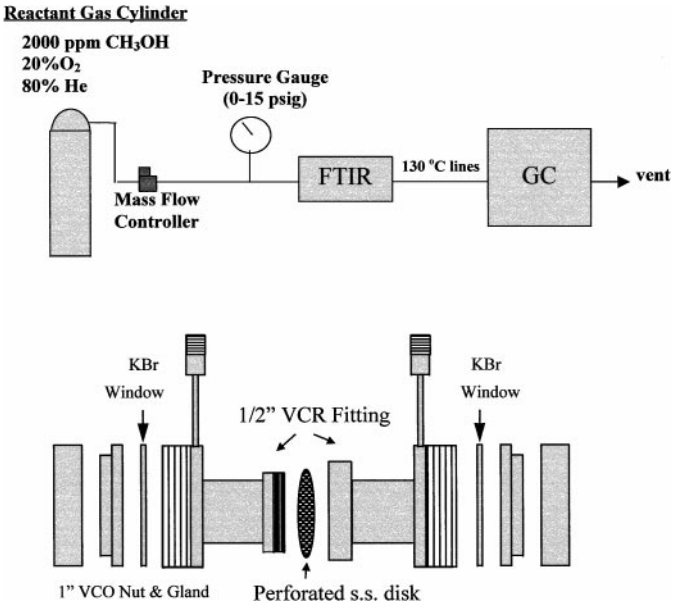

FIG. 2. Experimental apparatus and schematic diagram of the "fixed-bed" IR cell used in the present study.

using a specially designed *in situ* cell, which is described herein. Transmission mode was selected for this work due to the linear absorbance signal dictated by Beer's Law, and due to the inherent difficulties involved in quantitative reflectance methods such as DRIFTS (diffuse reflectance) and attenuated total reflectance (21, 44). Calibration of the IR signal for the adsorbed methoxylated surface species, which was reported elsewhere for these catalysts (18), was achieved by quantitatively dosing known amounts of methanol onto the catalysts at 110°C under vacuum (a special vacuum system for volumetric dosing was designed and constructed for this purpose).

The IR transmission cell was specially designed to provide a fixed-bed configuration during the *in situ* experiments. The design, made entirely of 316 stainless steel, is illustrated schematically in Fig. 2, where it can be seen that the cell is essentially a straight tube with gas inlet and outlet ports located as close to the KBr windows as possible to prevent dead space. Powdered catalyst samples were pressed into thin disks of perforated stainless steel sheet metal (distributed by McMaster–Carr; 30% open area, 0.008-in. thick, and using $\sim$5–30 mg of catalyst). Woven steel mesh was inadequate as a sample holder because its surfaces are not flat. The sample disks were then sealed with stainless steel gaskets inside the *in situ* IR cell using Cajon VCR fittings. The sample diameter exposed to the IR beam when the wafer is placed in the cell is 0.5 in.

The center of the cell is heated with standard heavy insulated heating tape. A thermocouple was placed in direct contact with the sample on the outside of the seal (i.e., the portion not exposed to reactant gas) by insertion through the VCR leak-port. The 32-mm KBr windows are affixed

by 1-in. VCO O-ring fittings (Cajon, Inc.). The O-rings are made of Viton and are, therefore, thermally stable to 204°C (maintaining the O-ring temperature below this threshold with water cooling permits catalyst sample temperatures of up to 450°C at the center of the cell). This method of window attachment has the advantage of easy removal for sample replacement, thermal stability, and it is leak-free from high vacuum to several atmospheres using only a finger-tight force on the VCO nut. To provide water cooling for the Viton O-rings and KBr windows, grooves were machined into the back faces of the 1-in. VCO bodies followed by subsequent surface sealing with a welded-on washer and welded insertion of 1/4-in. taps into the sealed groove for water inlet/outlet ports.

2.3. Experimental Procedure and Coupled GC Product Analysis

The following *in situ* experimental procedure was used. The samples were heated *in situ* to 350°C in flowing oxygen (3 mL/min; ultra high purity; JWS Technologies) and helium (12 mL/min; ultra high purity; JWS Technologies). The pretreated catalysts were then cooled to 100°C for acquisition of the clean catalyst spectrum followed by methanol introduction using a premixed oxidizing gas mixture of 2000 ppm methanol/20% O_2/80% He (Scott Specialty Gas Co.) with a flow rate of ∼30 mL/min (Brooks mass flow controller). The low concentration of gas-phase methanol was necessary to reduce gas-phase methanol signals in the *in situ* IR spectra. The temperature was then slowly ramped to various temperatures up to 300°C under the O_2/He/CH_3OH flow. Infrared spectra were obtained at each temperature after the signals had reached stable, steady-state values (∼10 min). The gas-phase methanol signal and clean catalyst signal were later subtracted from these spectra.

The product distributions from the IR cell were also obtained simultaneously with the *in situ* IR spectra using a Hach Carle Series 400 Gas Chromatograph (now EG&G Chandler Engineering). Only the flame ionization detector (FID) was used due to the extremely low 2000 ppm initial concentration of methanol, the FID signal at this concentration being still well above the minimum sensitivity. Typical products for methanol oxidation include formaldehyde (F), methyl formate (MF), dimethoxymethane, dimethylether (DME), and carbon oxides (CO_x) (3, 7–11). Response factors relative to methanol were determined by calibrated syringe injections for MF and dimethoxymethane, and the response factor for DME was found by flowing methanol over pure γ-alumina, which is known to be 100% selective to DME (3, 7–11). Unfortunately, formaldehyde has a very low FID response factor and, being experimentally present at concentrations that were also well below the thermal conductivity detector (TCD) detection limit, could not be measured directly. Instead, the sum of F + CO_x was found by using a carbon balance over the reactant and product streams. Gas lines between the cell exit and the GC were kept as short as possible and were heated to 120–130°C to prevent polymerization and condensation of the formaldehyde produced by the reaction. The experimental system is schematically shown in Fig. 2.

Catalyst weights were determined by a low temperature (100–150°C) calibration procedure as described. Direct measurement of the catalyst weight was not possible because the sealing gaskets always covered a portion of the catalyst-containing perforated metal sample disk and rendered some amount of catalyst inaccessible to the reaction gas. Instead, the *accessible* catalyst weight in the *in situ* IR cell was determined by first calculating with Beer's Law the amount (μmoles) of methanol adsorbed by the catalyst at a given low and nonreactive temperature. This calculation required knowledge of the total integrated area of the IR bands arising from the adsorbed methoxylated surface species (using the measured *in situ* IR spectrum, see Section 3), as well as the extinction coefficient obtained from previous chemisorption experiments (18). The accessible catalyst weight was then taken to be the weight that normalized the measured amount of adsorbed methanol to the known methoxylated surface site density (in μmoles/m^2 after unit conversion with BET surface area) obtained from the previous chemisorption experiments at the temperature of interest (18).

During the experiment, a 0–15 psig pressure gauge was used to measure the pressure drop across the catalyst bed, and a bubble flowmeter was used for measuring volumetric flow rates. Typically, a pressure drop of about 1 atm could be tolerated before blowing out catalyst from the holes of the perforated metal sample holder. High catalyst stability was also observed during methanol oxidation, since "cleaning" the used catalyst at 200–300°C in an O_2/He stream generated full recovery of the IR band intensities associated with the metal–oxygen double bonds of the active metal oxide surface species (see Ref. (21) for band assignments). This stability was expected for most supported metal oxide catalysts (42), but volatilization of vanadia surface species in 10% V_2O_5/SiO_2 has been observed during methanol oxidation under 4% CH_3OH in an O_2/He stream (45). The general stability of all catalysts tested in the present investigation is most likely due to the very low methanol concentrations used (2000 ppm in O_2/He), which appears to be insufficient for solvation and volatilization of the chemisorbed surface metal oxide species.

3. RESULTS

3.1. In Situ IR Spectra and Band Assignments

The *in situ* IR spectra of the adsorbed methoxylated surface species present on various metal oxide catalysts during steady-state methanol oxidation are presented in Figs. 3–7.

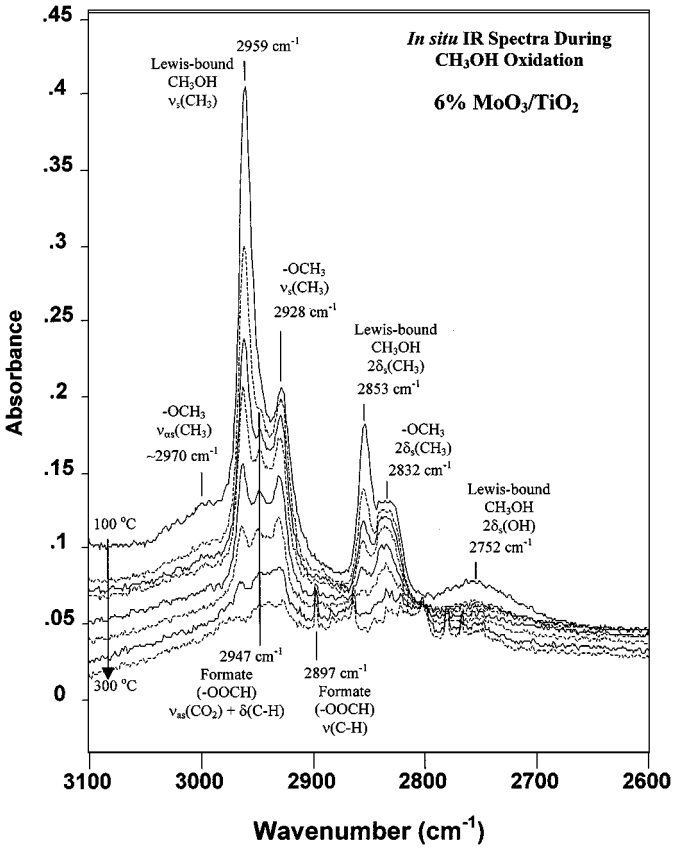

FIG. 3. *In situ* IR difference spectra of the C–H stretching region of 6% MoO_3/TiO_2 during methanol oxidation (2000 ppm methanol/20% O_2/80% He and ~30 mL/min total flow). The topmost spectrum corresponds to 100°C and the sequentially lower spectra correspond, respectively, to 150, 180, 200, 225, 250, 275, and 300°C.

In all cases, the clean catalyst and gas-phase methanol signals were subtracted from the raw IR spectra to isolate the signals of the adsorbed surface phases. The metal oxide loadings used for the supported metal oxide catalysts correspond to monolayer coverage, except for supported rhenia (higher loadings form volatile dimers) and for the active oxides supported on silica that cannot achieve monolayer coverages (higher loadings form bulk oxide microcrystallites) (42). These monolayer loadings were chosen to limit the number of bare oxide support sites on the catalyst surface; such sites can lead to the adsorption of undesired spectator methoxylated surface species that remain stable until ~300°C before decomposing into CO/CO_2 and water. As expected, the IR intensities of the adsorbed methoxylated surface intermediates decrease with increasing temperatures and will be quantitatively discussed.

The vibrational mode assignments for the adsorbed surface species on 6% MoO_3/TiO_2 are illustrated in Figs. 3 and 4. In the C–H stretching region, Fig. 3 indicates the presence of methoxylated surface species by the appearance of four intense, sharp bands at ~2959/2928 and ~2853/2832 cm^{-1}, as well as a weak and broad band at ~2752 cm^{-1}. In addition, three bands appear in the lower frequency region at 1455, 1445, and ~1361 cm^{-1} (see Fig. 4A). These modes are assigned by Lavalley *et al.* (46, 47) and Busca *et al.* (14, 48) to two distinct species that are each stable to high temperatures and evacuation: an intact, Lewis-bound surface methanol species and a dissociated surface methoxy species (OCH_3). The bands at 2928 cm^{-1} and 2832 cm^{-1} are assigned to the dissociated species and arise from Fermi resonance between the symmetric stretch (ν_s) and first overtone of the symmetric bend ($2\delta_s$) of CH_3 units in adsorbed OCH_3 species, respectively. The unusual intensity of these symmetric stretching bands is attributed to the Fermi resonance occurring between them (14, 46–48). The bands at 2959 and 2853 cm^{-1} are assigned to the same modes occurring in the undissociated, Lewis-bound CH_3OH species. A less-resolved and weaker shoulder around 2970 cm^{-1} is assigned to the asymmetric stretch (ν_{as}) of the CH_3 units in these two types of methoxylated surface species,

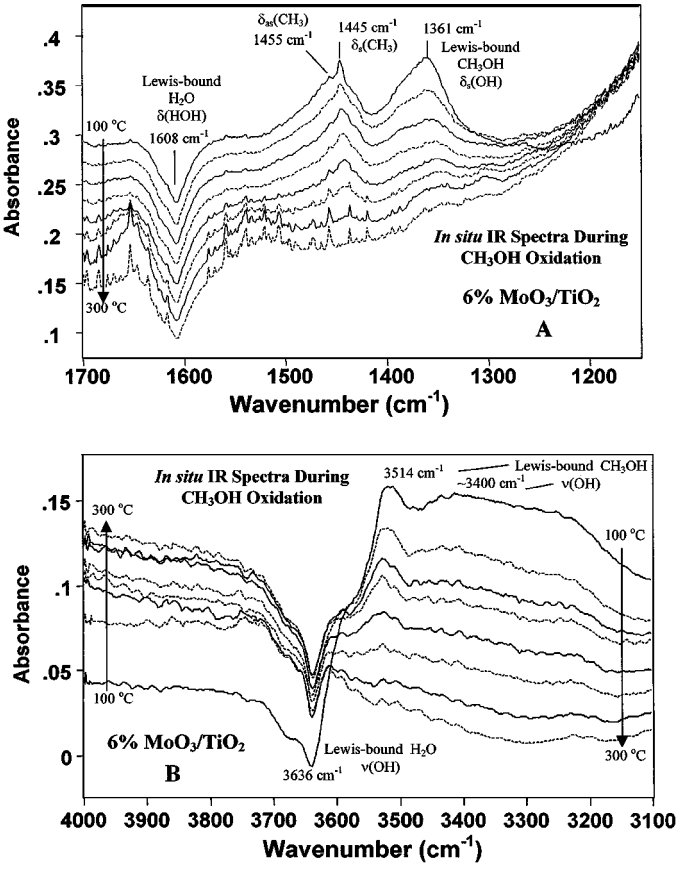

FIG. 4. (A) *In situ* IR difference spectra of the C–H bending/C–O stretching region of 6% MoO_3/TiO_2 during methanol oxidation (2000 ppm methanol/20% O_2/80% He and ~30 mL/min total flow). The topmost spectrum corresponds to 100°C and the sequentially lower spectra correspond, respectively, to 150, 180, 200, 225, 250, 275, and 300°C. (B) *In situ* IR difference spectra of the O–H stretching region of 6% MoO_3/TiO_2 during methanol oxidation (2000 ppm methanol/20% O_2/80% He and ~30 mL/min total flow). The temperatures vary as indicated and include 100, 150, 180, 200, 225, 250, 275, and 300°C.

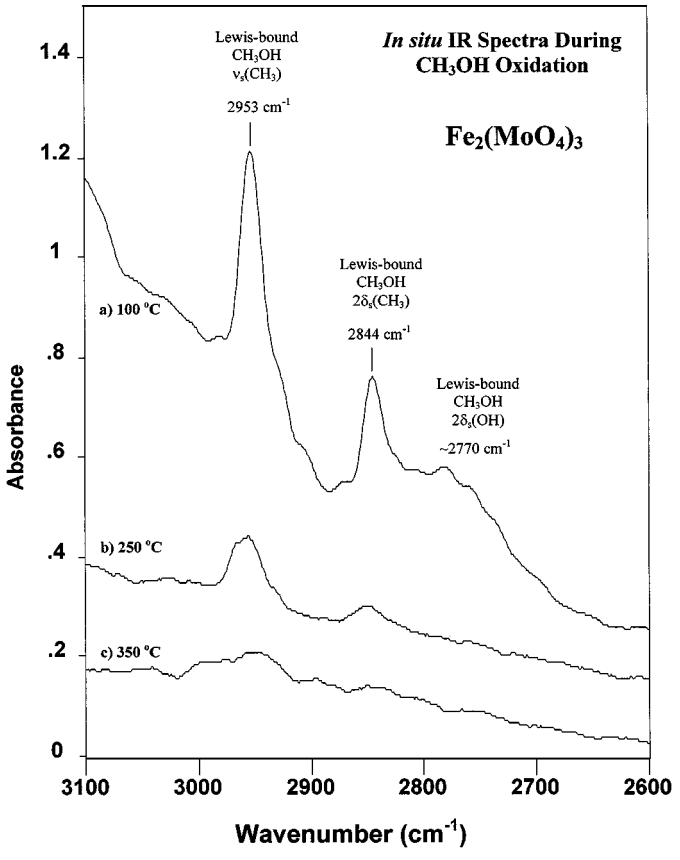

FIG. 5. *In situ* IR difference spectra of the C–H stretching region of $Fe_2(MoO_4)_3$ during methanol oxidation (2000 ppm methanol/20% O_2/80% He and ~30 mL/min total flow).

$(CH_3OH)_{ads}$ and $(CH_3O)_{ads}$. The low-frequency modes in the region 1430–1460 cm^{-1} in Fig. 4A are assigned to CH_3 bending vibrations at 1455 cm^{-1} (δ_{as}) and 1445 cm^{-1} (δ_s) that are not separately resolved between the two species.

Additional spectral IR features include a number of vibrational bands associated with the OH group of the intact, Lewis-bound methanol species: a band at ~1361 cm^{-1} due to the OH bending mode, δ(O–H); the overtone of this band, 2δ(O–H), at ~2752 cm^{-1}; and O–H stretching modes, ν(O–H), in the region 3100–3500 cm^{-1} (see Fig. 4B) (14, 46–48). Note that the assignment for the Lewis-bound methanol 2δ(OH) overtone band at ~2752 cm^{-1} is based on recent studies of methanol chemisorption onto WO_3 and WO_3/TiO_2 (surfaces known to exhibit Lewis acidity) (18). These studies showed that both the fundamental, δ(OH), and overtone, 2δ(OH), modes of the Lewis-bound methanol surface species increase and decrease together and in unison with the C–H stretching bands at 2853/2959 cm^{-1} of the same Lewis-bound methanol species when experimental conditions alter the surface concentration of this species. The IR bands at 1608 cm^{-1} (Fig. 4A) and 3636 cm^{-1} (Fig. 4B) are due, respectively, to the δ(H–O–H) and ν(OH) modes of strongly Lewis-bound water (49–51), which is present in small amounts on these catalysts even after evacuation at temperatures as high as 200°C. Their disappearance after methanol adsorption is indicated by a negative peak and demonstrates that the adsorption of methanol displaces Lewis-bound water. Also, the relative ratios of the Lewis-bound CH_3OH and dissociated CH_3O–species are seen to change depending on the catalyst. For example, supported molybdena catalysts contain comparable amounts of both species (Fig. 3), bulk $Fe_2(MoO_4)_3$ contains primarily the Lewis-bound intact species (Fig. 5), and supported vanadia catalysts contain mostly the dissociated surface methoxy species (Fig. 6). The bands at 2957 and 2856 cm^{-1} in the 10% V_2O_5/SiO_2 catalyst (Fig. 6) are due to methoxylated surface species adsorbed onto exposed silica surface sites.

The *in situ* IR spectra of 5% CrO_3/TiO_2 and 5% Re_2O_7/TiO_2 at 225°C are shown in Fig. 7 and have vibrational frequencies for the methoxylated surface species that are similar to those of 6% MoO_3/TiO_2 (i.e., bands at ~2959/2928, ~2853/2832, ~2752, 1455, 1445, and ~1361 cm^{-1} assigned as before). However, Fig. 7 also shows that the chromia–titania, rhenia–titania, and 3% V_2O_5/CeO_2 catalysts exhibit additional strong bands in the C–H and C–O stretching regions at reaction temperatures. These bands have been assigned to surface formate species (HCOO–)

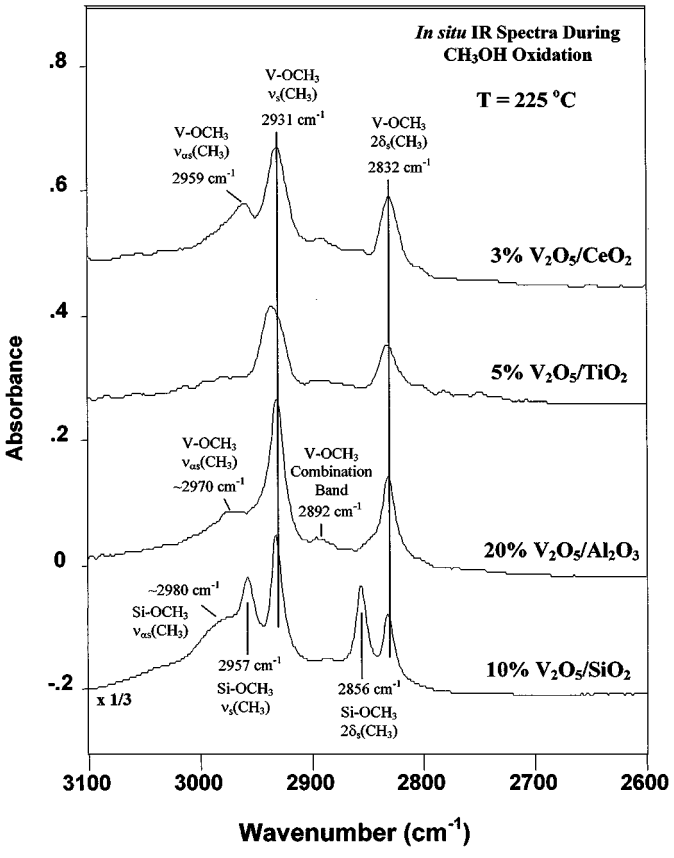

FIG. 6. *In situ* IR difference spectra (normalized to 10 mg) of the C–H stretching region of supported vanadia catalysts at 225°C during methanol oxidation (2000 ppm methanol/20% O_2/80% He and ~30 mL/min total flow).

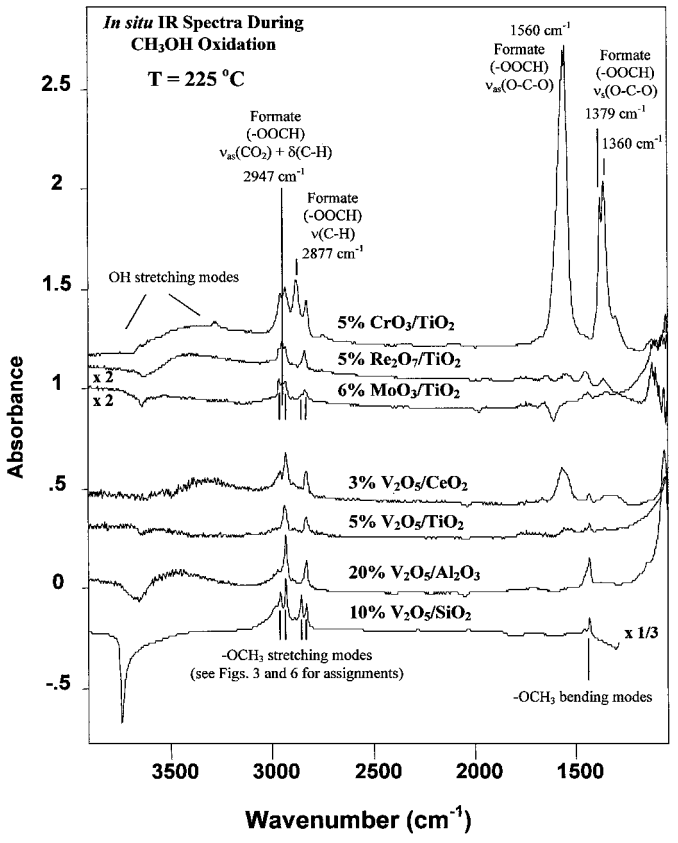

FIG. 7. Full-scale *in situ* IR difference spectra (normalized to 10 mg) of selected metal oxide catalysts at 225°C during methanol oxidation (2000 ppm methanol/20% O_2/80% He and ~30 mL/min total flow).

formed by the readsorption of formaldehyde product and correspond to bands at 1560 cm^{-1} (O–C–O asymmetric stretch) and 1360/1379 cm^{-1} (O–C–O symmetric stretch) (14, 46, 48). Higher frequency C–H stretching modes for the formate species appear at 2877 cm^{-1} and 2947 cm^{-1}, and their IR intensities relative to the C–O modes depend on the catalyst. In the case of 6% MoO_3/TiO_2 (Figs. 3 and 4), very weak formate bands are seen in the C–H stretching region at 2947 and 2897 cm^{-1}. Nevertheless, the band at 1361 cm^{-1} in Fig. 4A is almost certainly due to the hydroxyl bending mode, δ(OH), of intact adsorbed CH_3OH because there is no formate band at 1560 cm^{-1} and the 1361 cm^{-1} band is strongest at 100°C (where there is no significant reaction or formate production in the C–H region). Figure 7 also shows that methanol adsorption generally titrates the surface hydroxyls of the clean catalyst, as indicated by the negative bands above 3500 cm^{-1}.

3.2. Surface Concentrations of the Adsorbed Methoxylated Surface Species and Methanol Oxidation Catalytic Activity Data

From these IR data, the steady-state concentrations of the methoxylated surface intermediates were calculated by integrating the IR bands at ~2830–2850 cm^{-1} in the collected spectra. These IR bands represent both types of adsorbed CH_3OH and CH_3O– surface species, each being reactive for oxidation to CH_2O (see Section 4), and these IR bands have relatively little overlap with other vibrational bands in the spectra. Integrated molar extinction coefficients for these bands, which are the linear proportionality constants relating integrated IR areas to surface concentrations via Beer's Law, were taken from previous quantitative methanol chemisorption studies (18). This previous study also provided methanol chemisorption saturation site densities that can be used to calculate fractional surface coverages in the present work (see Table 1).

The fractional surface coverages of these methoxylated surface intermediates, as a function of the steady-state reaction temperature, are summarized in Fig. 8. The surface coverages decrease with increasing temperature, as expected because the adsorption equilibrium constant decreases with temperature whereas the reactivity of the methoxylated surface species simultaneously increases. Additionally, the surface coverages calculated using the total density of active surface metal atoms as the saturation site density are significantly lower than those using the methanol chemisorption site densities (see Table 1). In fact, only about one-third of the active surface metal atoms can simultaneously adsorb the methoxylated surface species at saturation due to lateral interactions, so the methanol chemisorption site densities are preferred for TOF calculations.

The catalytic activity data, obtained by online GC analysis, are presented in Figs. 9A and 9B, as well as in Table 2. The results in Fig. 9A reveal that below 250°C the methanol conversion is usually less than about 30%. Under these differential conditions the selectivity to formaldehyde remains quite high (see Table 2 and also note that CO_x is usually formed only at higher conversions from the overoxidation of readsorbed CH_2O (4, 7–11)).

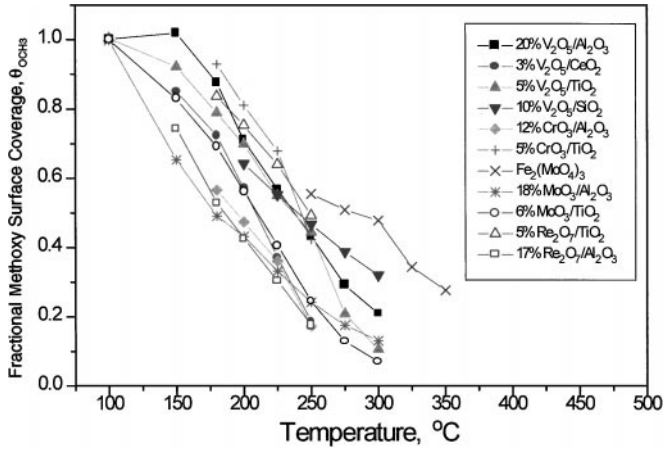

FIG. 8. Fractional surface coverage of adsorbed methoxylated intermediates as determined by *in situ* IR spectroscopy during steady-state methanol oxidation. Maximum site densities taken from previous methanol chemisorption experiments (18).

TABLE 1

Total Site Densities (from Static Experiments[a]) and Steady-State Concentrations of Methoxylated Surface Species during Methanol Oxidation at 225°C

Catalyst	Site density			Methanol oxidation (225°C)		
	Methanol Chemisorption [$N_{sat} = \mu$mol OCH_3/m^2]	Surface active metal atoms [$N_{metal} = \mu$mol metal atoms/m^2]	Relative density (N_{sat}/N_{metal}) [molecules OCH_3/metal atom]	Steady-state methoxy concentration [$N = \mu$mol OCH_3/m^2]	Fractional surface coverage [θ_{OCH_3} (chemisorption)]	Fractional surface coverage [$\theta_{OCH_3,m}$ (metal sites)]
20% V_2O_5/Al_2O_3	3.64	12.22	0.30	2.06	0.57	0.17
3% V_2O_5/CeO_2	2.68	9.17	0.29	0.99	0.37	0.11
5% V_2O_5/TiO_2	3.44	10.00	0.34	1.89	0.55	0.19
10% V_2O_5/SiO_2	0.93	3.44	0.27	0.51	0.55	0.15
12% CrO_3/Al_2O_3	3.91	6.67	0.59	1.41	0.36	0.21
5% CrO_3/TiO_2	4.95	9.09	0.54	3.35	0.68	0.37
$Fe_2(MoO_4)_3$	2.50	na[b]	na	1.44	0.58	na
18% MoO_3/Al_2O_3	2.18	7.72	0.28	0.72	0.33	0.094
6% MoO_3/TiO_2	1.35	6.83	0.20	0.55	0.41	0.080
17% Re_2O_7/Al_2O_3	1.96	3.90	0.50	0.59	0.30	0.15
5% Re_2O_7/TiO_2	1.58	3.98	0.40	1.01	0.64	0.25

[a] Site density values taken from Ref. (18).
[b] na = not applicable.

Interestingly, very little DME was formed over the alumina-supported metal oxides, despite their reported DME selectivities of 50% or more at similar temperatures under 6% methanol in O_2/He (4, 7–11). The minimal production of DME in the present study is almost certainly attributable to the much lower gas-phase methanol concentration currently used (2000 ppm or 0.2% methanol in O_2/He), because DME formation is a bimolecular reaction between two surface methoxy groups with a rate proportional to the square of methanol concentration (Ref. (52), kinetic Model no. 3). Note also that whereas temperature distributions within the catalyst sample wafers were not directly measured, the perforated metal disks into which the catalysts have been pressed would be expected to greatly facilitate a uniform temperature distribution via fast heat conductance from the uniformly and radially heated metal cell wall. Additionally, the *empty* perforated metal sample holders did not exhibit any appreciable activity at the temperatures used in the present study. The methanol oxidation activity and selectivity data were then used to calculate the TOFs to redox products (MF+F) in the fixed-bed IR cell by normalizing the redox activities to the number of active sites determined from methanol chemisorption. These TOFs are given graphically in Fig. 9B as a function of temperature.

TABLE 2

Activity and Selectivity Data for Methanol Oxidation over Metal Oxide Catalysts under Conditions of Differential Conversion

Catalyst	Conversion (%)	Temperature (°C)	Activity (mol/g/h)	Selectivity (%)		
				F+CO_x	MF	DME
20% V_2O_5/Al_2O_3	15	225	2.45 e−03	97	0	3
3% V_2O_5/CeO_2	23	200	1.45 e−03	95	5	0
5% V_2O_5/TiO_2	18	200	3.05 e−03	95.2	4.4	0.4
10% V_2O_5/SiO_2	19	225	1.23 e−03	100	0	0
12% CrO_3/Al_2O_3	15	200	3.49 e−03	90	9.3	0.7
5% CrO_3/TiO_2	13	200	1.34 e−03	85	15	0
$Fe_2(MoO_4)_3$	14	275	7.08 e−04	83	0	17
18% MoO_3/Al_2O_3	16	225	1.91 e−03	68	0	32
6% MoO_3/TiO_2	23	225	1.80 e−03	89.6	9	1.4
17% Re_2O_7/Al_2O_3	21	200	4.10 e−03	72	0	28
5% Re_2O_7/TiO_2	14	200	6.92 e−04	90	8	2

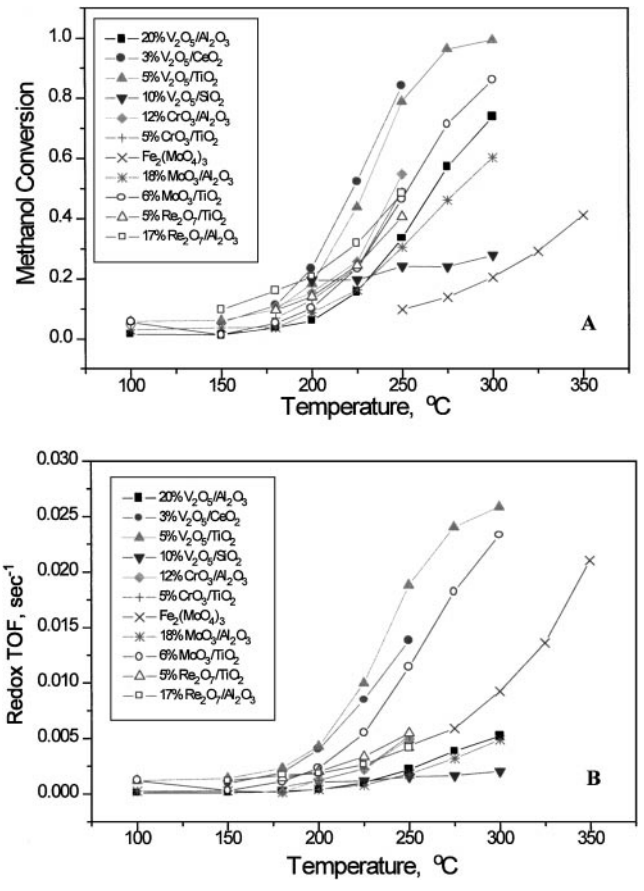

FIG. 9. Kinetic data at various temperatures obtained from GC analysis of the product stream exiting the fixed-bed IR cell during steady-state methanol oxidation: (A) methanol conversions and (B) TOFs (normalized to methanol chemisorption site densities (18)).

4. DISCUSSION

4.1. Preliminary Comments

The mechanistic origin of the ligand effect in metal oxide catalysts may now be considered by combining the previously described results with the kinetic expressions predicted by the reaction mechanism. In particular, the quantification of the adsorbed methoxylated surface intermediates, $(CH_3OH)_{ads} + (CH_3O)_{ads}$, by *in situ* IR spectroscopy enables the adsorption and surface reaction steps to be decoupled, because the usual requirement of expressing all kinetic equations in terms of gas-phase species has now been relaxed. Of course, a prerequisite for such an analysis is that the quantified adsorbed species must be true intermediates in the reaction. For many molybdena and vanadia systems, the dissociated surface methoxy species have been shown by temperature-programmed desorption (TPD) and IR techniques to be reactive intermediates in the selective oxidation of methanol to formaldehyde (14, 21).However, the role of the Lewis-bound methanol species is less clear.

Farneth *et al.* (53) found that the TPD spectrum of methanol adsorbed at 25°C on MoO_3 produced two methanol peaks, the first at 120°C and the second at 220°C. A formaldehyde peak was only observed in conjunction with the higher temperature peak. They associated the Lewis-bound surface methanol species with the low temperature (nonreactive) methanol TPD peak, whereas the high temperature (reactive) methanol TPD peak was assigned to recombination of dissociated surface methoxy species with adjacent surface OH groups. The initial room temperature adsorption of methanol would be expected to yield a large desorption peak of weakly held surface methanol species at low temperatures (majority of peak area below 150°C). However, the methoxylated surface species present at higher (reaction) temperatures, which are reactive intermediates for formaldehyde production, cannot be assigned solely to the dissociated methoxy species.

Specifically, the present IR results clearly indicate the existence of Lewis-bound surface methanol species on molybdena catalysts at reaction temperatures exceeding 200°C (see Figs. 3 and 5; vanadia catalysts possess only dissociated methoxy species at all temperatures above 100°C). Moreover, the commercial $Fe_2(MoO_4)_3$ catalyst for methanol oxidation exhibits IR bands assigned exclusively to the Lewis-bound surface methanol species (Fig. 5) and is active to formaldehyde. Recent methanol chemisorption IR experiments have also shown that Lewis-bound surface methanol species coexist in significant amounts with the dissociated methoxy surface species when adsorbed on bulk and supported molybdena catalysts at a temperature high enough (110°C) to prevent weak physical adsorption (18). Therefore, it seems probable that this Lewis-bound methanol species is also a reactive intermediate for methanol oxidation to formaldehyde, in addition to the dissociated methoxy surface species, and a plausible mechanism for this reaction pathway is given in Section 4.2.

Finally, the presence of stable (unreactive) methoxylated spectator species, which can be formed by the direct adsorption of methanol onto the oxide supports, has been largely eliminated through the use of monolayer coverages of the active surface metal oxides. Spectator species are stable on the surface until well above 300°C before decomposing to CO, CO_2, and H_2O and should not be counted as reactive intermediates in the production of formaldehyde. Titration and removal of the adsorption sites on the oxide supports at monolayer surface coverages of supported metal oxides are confirmed by comparative chemisorption IR experiments (18), in which monolayer catalysts and pure oxide supports were found to exhibit distinctly different IR band frequencies for their respective methoxylated surface species. Also, transient IR flow experiments over supported vanadia monolayer catalysts (21), in which methanol was suddenly removed from the feed stream, resulted in the complete loss of methoxylated IR signals within seconds

at 225°C and indicates that these methoxylated surface species are true intermediates and not spectators.

In the present study, however, it was impossible to achieve monolayer surface coverages in the 10% V_2O_5/SiO_2 catalyst or in the supported rhenia catalysts. Fortunately, for the vanadia/silica system, it was possible to selectively isolate and quantify the surface vanadia-methoxylated intermediates because the surface silica-methoxylated spectators possessed IR bands at distinctly different frequences (see Fig. 6). Moreover, the supported rhenia catalysts were found to exhibit IR bands only associated with the surface methoxylated species coordinated to rhenia (see Fig. 7 and Ref. 18)—alumina or titania surface methoxylated species were not detected, possibly due to blocking of the support sites by steric hinderance of the surface rhenia-methoxylated species. Similar selective adsorption was also found in $Fe_2(MoO_4)_3$, in which only Mo-methoxylated intermediates were detected but not iron-methoxylated species (see Fig. 5 and Ref. 18). Therefore, the measured surface concentrations of the observed methoxylated species may be taken as the true intermediate concentrations for all of the catalytic systems tested in the present study.

4.2. Reaction Mechanism and Kinetics

The mechanism and apparent overall kinetics of methanol oxidation to formaldehyde have been previously described in detail using a variety of different mechanistic assumptions (9, 14, 48, 53–55). A Langmuir–Hinshelwood approach is generally taken to separately describe the adsorption, surface reaction, and desorption steps. However, the kinetic derivations in the literature generally assume that methanol oxidation occurs only through dissociatively adsorbed methoxy species and that methoxy surface coverages are low compared to the total number of adsorption sites. The results of the present study indicate that these assumptions are not always applicable, because the Lewis-coordinated methanol species is also a reactive intermediate and the total fractional surface coverages of methoxylated intermediates are between 0.3 and 0.6 at a reaction temperature of 225°C (see Table 1; total site densities based on methanol chemisorption (18)). Therefore, the previous kinetic models must be adjusted to account for this new mechanistic information, as is shown in the following equations (S = V, Mo, or other metal cation in the active metal oxide; S' = metal cation in the oxide support):

Overall Stoichiometry

$$CH_3OH + 1/2\ O_2 = CH_2O + H_2O, \qquad [1]$$

Langmuir–Hinshelwood Reaction Steps

$$CH_3OH + (O_mS\text{–}) + (\text{–O–}S'O_n) \leftrightarrow CH_3O\text{–}SO_m + HO\text{–}S'O_n, \quad K_1, \qquad [2]$$

$$CH_3OH + (O_mS\text{–}) + (\text{–O–}S'O_n) \leftrightarrow ((CH_3OH)_{LC}\text{–}SO_m) + (\text{–O–}S'O_n), \quad K_2, \qquad [3]$$

$$CH_3O\text{–}SO_m \rightarrow CH_2O + H\text{–}SO_m, \quad k_3, \qquad [4]$$

$$((CH_3OH)_{LC}\text{–}SO_m) + (\text{–O–}S'O_n) \rightarrow CH_2O + H\text{–}SO_m + HO\text{–}S'O_n, \quad k_4, \qquad [5]$$

$$H\text{–}SO_m + 2(\text{–O–}S'O_n) \leftrightarrow (O_mS\text{–}) + (\text{–O–}S'O_n) + HO\text{–}S'O_n, \quad K_5, \qquad [6]$$

$$2(HO\text{–}S'O_n) \leftrightarrow H_2O + (\text{–O–}S'O_n) + (\text{–O–}S'O_{n-1}), \quad K_6, \qquad [7]$$

$$O_2 + 2(\text{–O–}S'O_{n-1}) \leftrightarrow 2(\text{–O–}S'O_n), \quad K_7, \qquad [8]$$

Site Balance

$$[SO_m] = S_{T1} - [CH_3O\text{–}SO_m] - [(CH_3OH)_{LC}\text{–}SO_m] - [H\text{–}SO_m], \qquad [9]$$

$$[O\text{–}S'O_n] = S_{T2} - [HO\text{–}S'O_n] - [\text{–O–}S'O_{n-1}]. \qquad [10]$$

As in previous models, this mechanism initially involves the chemisorption of methanol to form reactive surface intermediates. A surface hydroxyl group is also produced upon dissociative adsorption, whereas only the Lewis-coordinated complex is formed for intact chemisorption. Both types of surface methoxylated intermediates subsequently decompose into gas-phase formaldehyde and a surface hydroxyl. The surface hydroxyls then recombine and desorb as water. Furthermore, the catalytic surface reaction itself follows a mechanism similar to the Mars–Van Krevelen pathway, in which the adsorbed methoxylated intermediates decompose without gas-phase oxygen. Instead, gas-phase oxygen serves only to reoxidize the reduced catalyst by supplying a "pool" of adsorbed surface active oxygen species. Nonselective side reactions include the formation of DME on strongly Lewis acidic and nonredox metal oxide sites such as alumina and titania exposed support sites, as well as readsorption of formaldehyde to surface formate species, which decompose to CO and CO_2 (4, 7–11, 14).

The reaction kinetics may be derived from these mechanistic equations with the knowledge that the surface decomposition of the adsorbed methoxylated surface intermediates is the rate-determining step (known from kinetic isotope experiments) (55). Thus, the rate of the overall reaction is derived from Eqs. (4) and (5) as follows:

$$\text{Rate} = \{k_3 \times [CH_3O\text{–}SO_m]\} + \{k_4 \times [((CH_3OH)_{LC}\text{–}SO_m)] \times [(\text{–O–}S'O_n)]\}. \qquad [11]$$

Further simplification can be made by assuming that the availability of surface oxide support sites, $(\text{–O–}S'O_n)$, for hydroxyl group formation in reaction (5) is probably quite high relative to the concentration of $((CH_3OH)_{LC}\text{–}SO_m)$

sites, since several oxide support sites surround each active metal oxide site (42). As a result, the concentration of oxide support sites, $[(-O-S'O_n)]$, may be taken to be pseudo-zero-order and can be factored into an apparent rate constant, $k_{4,app}$, which, in similarity with k_3, is primarily a function of the hydride transfer ability of the active metal oxide site. Moreover, it is also very likely that the two types of methoxylated surface intermediates, $((CH_3OH)_{LC}-SO_m)$ and CH_3O-SO_m, decompose at roughly the same apparent rate, that is, k'_{rds} (rds = rate-determining step) $= k_3 \sim k_{4,app}$, considering that a similar hydride transfer mechanism and transition state most likely occur in each case.

Under these assumptions, the methanol oxidation reaction rate toward formaldehyde may be written as

$$\text{Rate} = k'_{rds} \times \{[CH_3O-SO_m] + [((CH_3OH)_{LC}-SO_m)]\}. \quad [12]$$

Expressions for the concentrations of methoxylated surface intermediates are then found by using the equilibrium relationships given in the reaction mechanism (Eqs. [2]–[3] and [6]–[10]):

$$[CH_3O-SO_m] = \frac{K_1[CH_3OH]}{K_6^{1/2}[H_2O]^{1/2}K_7^{1/4}[O_2]^{1/4}} \cdot [SO_m], \quad [13]$$

$$[((CH_3OH)_{LC}-SO_m)] = K_2[CH_3OH][SO_m], \quad [14]$$

$$[SO_m] = \frac{S_{T1}}{1 + \left(\frac{K_6^{1/2}[H_2O]^{1/2}}{K_5K_7^{1/4}[O_2]^{1/4}}\right) + \left(\frac{K_1K_7^{1/4}[O_2]^{1/4}}{K_6^{1/2}[H_2O]^{1/2}} + K_2\right)[CH_3OH]}. \quad [15]$$

Combining Eqs. [13]–[15] and performing some algebraic manipulation yields an expression for the total fractional surface coverage of the methoxylated surface intermediates:

$$\theta_m = \frac{[CH_3O-SO_m] + [((CH_3OH)_{LC}SO_m]}{S_{T1}} = \frac{K_{ads}P_{CH_3OH}}{1 + K_{ads}P_{CH_3OH}} \quad [16a]$$

where

$$K_{ads} = \left(\frac{K_1K_7^{1/4}(P_{O_2})^{1/4}}{K_6^{1/2}(P_{H_2O})^{1/2}} + K_2\right) \cdot \left(1 + \frac{K_6^{1/2}(P_{H_2O})^{1/2}}{K_5K_7^{1/4}(P_{O_2})^{1/4}}\right)^{-1}. \quad [16b]$$

Finally, the methanol oxidation TOF may be represented as

$$\text{TOF} = (k_{rds} \cdot \theta_m) = k_{rds} \cdot \frac{K_{ads}P_{CH_3OH}}{1 + K_{ads}P_{CH_3OH}}. \quad [17]$$

The parameters in this rate expression have the following units: TOF and k_{rds} in s^{-1}, K_{ads} in $Torr^{-1}$, and P_{CH_3OH} in Torr. The adsorption isotherm, which is Langmuir in form, may be expressed equivalently in terms of methanol concentration (mol/L), in which case K_{ads} has units of L/mol. Of course, an important caveat with this model concerns the fact that the adsorption equilibrium constant, K_{ads}, is really only constant as long as the water and oxygen partial pressures remain constant, as will be discussed in more detail.

4.2.1. Comparison with other kinetic models. The kinetic model derived previously is very similar in form to the rate expression presented by Zhang *et al.* (54) for ethanol oxidation to acetaldehyde over uniform oxide surfaces (nonuniform surfaces having more complicated rate expressions as shown by these authors). However, in their mechanism Zhang *et al.* assumed that only dissociated ethoxy species were reactive intermediates and, also, that further simplification of their rate expression is possible by assuming low surface coverages of the ethoxy and hydroxyl surface species. The resulting simplified rate equation was then used to explain product inhibition by water, which has been empirically shown to lower the rates of ethanol oxidation under high moisture conditions (54). Similarly, Holstein and Machiels (55) have recently derived a kinetic expression applicable to "wet" methanol oxidation conditions, for which product inhibition by water vapor has also been empirically observed. As with the simplified Zhang model, the Holstein and Machiels mechanism considers only dissociatively adsorbed methoxy species as reactive intermediates in methanol oxidation, and also that surface methoxy and hydroxyl coverages are sufficiently low for the concentration of adsorption sites to remain high and roughly constant.

In the present model, these assumptions correspond to setting $K_2 = 0$ and assuming that $K_{ads}P_{CH_3OH} \ll 1$ (low surface methoxy coverage) and that $(K_6P_{H_2O})^{0.5} \ll 1$ (low surface hydroxyl coverage). Application of these restrictions to Eqs. [16] and [17] results in the following expressions, which are identical to those presented by Zhang *et al.* for ethanol oxidation (54) and by Holstein and Machiels for methanol oxidation (55):

$$\theta_{OCH_3} = \frac{K_7^{1/4}P_{O_2}^{1/4}K_1P_{CH_3OH}}{K_6^{1/2}P_{H_2O}^{1/2}}, \quad [18]$$

$$\text{TOF} = k_{rds} \cdot \frac{K_7^{1/4}P_{O_2}^{1/4}K_1P_{CH_3OH}}{K_6^{1/2}P_{H_2O}^{1/2}}. \quad [19]$$

The reaction orders for the vapor-phase species present during methanol oxidation have also been empirically tested by deliberately varying the partial pressures of the feed gases (55). Some model deviation was indicated by the empirical orders of 0.94 for methanol, 0.10 for oxygen, and

−0.45 for water that may be related to the assumption of low surface coverage and its corresponding form of rate equation.

Under the "dry" conditions typically found in single-pass differential reactors, such as the fixed-bed IR cell used in the present study, both the full kinetic model (Eqs. [16] and [17] and its low surface coverage form (Eq. [19]) predict that the TOF is much more dependent on the methanol concentration (first order) than on the water vapor concentration (negative one-half order). Thus, for the low concentrations of water vapor produced at differential methanol conversions (water being absent from the feed), the weak dependence of TOF on water concentration may be considered roughly constant. Moreover, methanol oxidation over oxide catalysts is generally performed in a large excess of oxygen (2, 3), effectively maintaining a constant partial pressure of oxygen. Under these conditions, K_{ads} in Eq. [17] is also roughly invariant with methanol partial pressure and represents an apparent Langmuir adsorption constant for methanol.

This "dry" model may also be simplified to the condition of low surface coverage, in which $K_{ads}P_{CH_3OH} \ll 1$, to yield the following expression:

$$\text{TOF} = k_{\text{overall}} \times P_{CH_3OH},$$

where

$$k_{\text{overall}} = K_{ads} \times k_{rds}. \qquad [20]$$

Deo and Wachs (7) have shown that Eq. [20] is valid at a given partial pressure of methanol under the moisture-free differential conditions described previously. They calculate methanol oxidation activation energies over supported vanadia catalysts in a moisture-free single-pass plug flow reactor (PFR) to be ~20 kcal/mol—the same value obtained by Holstein and Machiels (55) in a water-inhibited multipass reactor when the inhibition is taken into account. However, whereas the concentration of surface hydroxyl sites remains very low under these dry conditions (due to both the easy desorption of water and its easy displacement by methanol), the concentrations of surface methoxylated species are known to be significant from the present IR results ($\theta_m > 0.3$ at 225°C). This limits the predictive range of methanol partial pressures for which the rate constants are applicable using the low surface coverage model given by Eq. [20]. For example, the TOF will not increase to infinity with increased methanol partial pressure but will level out once the catalyst surface is saturated with methoxylated intermediate species. The advantage of the full model given by Eq. [17] lies in its ability to predict methanol oxidation kinetic behavior at all surface intermediate coverages while also accounting for both types of methoxylated surface intermediate species.

4.3. Decoupled Kinetics and the Origin of the Ligand Effect in Metal Oxides

Using the kinetic model given by Eq. [17] and the experimental data presented in the previous section, it is now possible to decouple the adsorption and surface decomposition steps during methanol oxidation over metal oxide catalysts. The results of such calculations are given in Table 3, where comparisons are made between several different assumptions. Specifically, the effect of simplifying the Langmuir adsorption isotherm (Eqs. [16] and [17]) to its linear form shown in Eq. [20] is compared for calculations using methanol chemisorption site densities in one case and total active metal site densities in the other case. The Arrhenius equations used in calculating the preexponential factors, apparent heats of methanol adsorption, activation energies for decomposition of surface methoxylated intermediates, and entropies of transition are given in the Appendix.

In traditional fixed-bed kinetic experiments, an apparent activation energy of 18–22 kcal/mol is usually observed for these catalysts under differential conditions and in the absence of mass transfer limitations (3, 7, 9). For comparison, the corresponding apparent activation energy for the overall reaction in the present fixed-bed IR study may be calculated from the values shown in Table 3 as $E_{\text{apparent}} = E_a + \Delta H_{\text{ads,linear}}$, using total metal site densities and a linear kinetic expression (Eq. [20]) to be consistent with the literature calculations. The apparent activation energy calculated in this way averages about 15–18 kcal/mol, which is quite similar to the literature value. Therefore, it may be concluded that the novel fixed-bed IR cell used in the present study has significantly diminished the mass transfer limitations in the porous catalytic sample disks. This conclusion is further supported in the vanadia and molybdena catalysts by the lack of significant surface formate production (Fig. 7), which occurs by readsorption of the formaldehyde product and has been previously shown to be enhanced in the presence of mass transfer limitations (21).

An exception is the vanadia/silica catalyst, which has an apparent activation energy of less than 10 kcal/mol and clearly experiences large mass transfer effects despite its very low TOF. The most likely explanation for this effect is an increase in the tortuousity of the high surface area silica support (320 m^2/g) after compression of the vanadia/silica samples into the perforated disk sample holder. Previous equilibrated adsorption studies (18, 21) indicate that most catalysts have the same total uptake of methanol at saturation irrespective of whether they are prepared as compressed wafers or as loose powders (i.e., all sites are accessible). However, diffusion limitations can still occur during kinetic experiments on such compressed wafers if the gaseous path becomes sufficiently tortuous, the tortuousity becoming more severe with higher surface areas. Fortunately, the other

TABLE 3

Adsorption Equilibrium and Surface Reaction Kinetic Constants during Steady-State Methanol Oxidation at 225°C

Calculations Using Methanol Chemisorption Site Densities

Catalyst	TOF (chemisorption) (s^{-1})	Linear isotherm A_{ads} (L/mol)	Linear isotherm ΔH_{ads} (kcal/mol)	Linear isotherm K_{ads} (L/mol)	Langmuir isotherm A_{ads} (L/mol)	Langmuir isotherm ΔH_{ads} (kcal/mol)	Langmuir isotherm K_{ads} (L/mol)	Surface methoxy decomposition A (s^{-1})	Surface methoxy decomposition E_a (kcal/mol)	Surface methoxy decomposition k_{rds} (s^{-1})	Surface methoxy decomposition $\Delta S^{\ddagger}$ (498 K) (kcal/mol/K)
V/Al	9.76 e−04	50.55	−4.85	6.80 e+03	0.16	−11.41	1.61 e+04	1.31 e+07	22.52	1.71 e−03	−0.0270
V/Ce	8.45 e−03	31.55	−5.07	5.30 e+03	0.00349	−14.42	7.44 e+03	2.89 e+07	20.82	2.10 e−02	−0.0254
V/Ti	9.97 e−03	71.39	−4.50	6.74 e+03	0.08	−12.00	1.49 e+04	1.68 e+07	20.43	1.81 e−02	−0.0265
V/Si	1.15 e−03	194.78	−3.51	6.76 e+03	11.1	−7.14	1.50 e+04	2.85 e+01	9.43	2.07 e−03	−0.0529
Cr/Al	2.19 e−03	46.50	−4.51	4.43 e+03	1.47	−8.37	6.93 e+03	1.08 e+11	29.95	7.74 e−03	−0.0091
Cr/Ti	2.25 e−03	444.27	−2.92	8.50 e+03	5.66e−07	−23.72	1.46 e+04	1.70 e+05	17.45	3.73 e−03	−0.0356
FeMo	1.57 e−03	18.54	−6.44	1.24 e+04	2.51	−9.32	3.09 e+04	4.20 e+05	19.22	1.54 e−03	−0.0338
Mo/Al	7.75 e−04	5.28	−6.57	4.04 e+03	0.56	−9.19	6.04 e+03	5.68 e+07	23.66	2.35 e−03	−0.0241
Mo/Ti	5.42 e−03	23.22	−5.32	5.02 e+03	0.0558	−11.79	8.34 e+03	2.39 e+07	21.10	1.31 e−02	−0.0258
Re/Al	2.62 e−03	0.04	−11.30	3.83 e+03	0.00182	−14.73	5.31 e+03	1.21 e+07	20.84	8.64 e−03	−0.0271
Re/Ti	3.32 e−03	32.62	−5.42	7.80 e+03	0.0715	−12.49	2.17 e+04	3.93 e+04	15.67	5.21 e−03	−0.0385

Calculations Using Metal Atom Site Densities

Catalyst	TOF (Metal Atom) (s^{-1})	Linear isotherm A_{ads} (L/mol)	Linear isotherm ΔH_{ads} (kcal/mol)	Linear isotherm K_{ads} (L/mol)	Langmuir isotherm A_{ads} (L/mol)	Langmuir isotherm ΔH_{ads} (kcal/mol)	Langmuir isotherm K_{ads} (L/mol)	Surface methoxy decomposition A (s^{-1})	Surface methoxy decomposition E_a (kcal/mol)	Surface methoxy decomposition k_{rds} (s^{-1})	Surface methoxy decomposition $\Delta S^{\ddagger}$ (498 K) (kcal/mol/K)
V/Al	2.91 e−04	15.05	−4.85	2.02 e+03	6.76	−5.82	2.42 e+03	1.31 e+07	22.52	1.71 e−03	−0.0270
V/Ce	2.47 e−03	9.22	−5.07	1.55 e+03	3.17	−6.25	1.75 e+03	2.89 e+07	20.82	2.10 e−02	−0.0254
V/Ti	3.43 e−03	24.55	−4.50	2.32 e+03	8.81	−5.72	2.85 e+03	1.68 e+07	20.43	1.81 e−02	−0.0265
V/Si	3.10 e−04	52.69	−3.51	1.83 e+03	35.24	−4.07	2.15 e+03	2.85 e+01	9.43	2.07 e−03	−0.0529
Cr/Al	1.28 e−03	27.27	−4.51	2.60 e+03	6.51	−6.17	3.32 e+03	1.08 e+11	29.95	7.74 e−03	−0.0091
Cr/Ti	1.23 e−03	241.90	−2.92	4.63 e+03	26.68	−5.54	7.21 e+03	1.70 e+05	17.45	3.73 e−03	−0.0356
FeMo	na	na	na	na	na	na	na	na	na	na	na
Mo/Al	2.19 e−04	1.49	−6.57	1.14 e+03	0.92	−7.15	1.27 e+03	5.68 e+07	23.66	2.35 e−03	−0.0241
Mo/Ti	1.07 e−03	4.59	−5.32	9.92 e+02	2.64	−5.95	1.08 e+03	2.39 e+07	21.10	1.31 e−02	−0.0258
Re/Al	1.31 e−03	0.02	−11.27	1.87 e+03	0.0055	−12.77	2.21 e+03	1.21 e+07	20.84	8.64 e−03	−0.0271
Re/Ti	1.32 e−03	12.96	−5.42	3.10 e+03	3.59	−6.98	4.15 e+03	3.93 e+04	15.67	5.21 e−03	−0.0385

Note. na = not applicable.

somewhat lower surface area catalysts apparently maintained sufficient interparticle void space after compression to avoid such mass transfer limitations in the present study.

Table 3 also shows that the activation energies for the surface decomposition step are independent of the choice of adsorption isotherm and average about 20 kcal/mol, consistent with the energy required for C–H bond breaking that occurs during this reaction step (55). Additionally, the choice of isotherm has relatively little effect on the calculated heats of adsorption when using metal-based site densities, the ΔH_{ads} values being roughly −5 kcal/mol for both the linear (Eq. [20]) and Langmuir (Eq. [16a]) isotherms. However, use of the methanol chemisorption site densities resulted in substantial differences in the calculated heats of adsorption between the two different isotherms: about −5 kcal/mol for the linear isotherm and higher ΔH_{ads} values of roughly −10 kcal/mol for the Langmuir isotherm. Therefore, simplification of the adsorption isotherm to a linear proportionality (low surface coverage assumption) is not valid if methanol chemisorption site densities are used in the kinetic calculations. Moreover, the fact that the site densities have such a dramatic effect on the heats of adsorption further suggests that the methanol chemisorption site densities should be used rather than the metal site densities, which are clearly overestimating the adsorption affinities (underestimating θ_{OCH_3}) for these catalysts during actual reaction conditions.

Indeed, Tables 3 and 4 and Figs. 10A and 10B provide a clear example of the importance of using the full Langmuir

TABLE 4

Comparison of TOFs Measured with IR and Fixed-Bed Experiments for a Feed Methanol Concentration of 1.46×10^{-3} mol/L (45.6 Torr) at 225°C[a]

Catalyst	Fixed-bed TOF s^{-1}	Ref.	IR TOF s^{-1}
20% V_2O_5/Al_2O_3	6.59 e−03	9, 57	1.34 e−03
3% V_2O_5/CeO_2	2.05 e−01	9, 58	1.52 e−02
5% V_2O_5/TiO_2	1.34 e−01	9, 58	1.46 e−02
10% V_2O_5/SiO_2	5.22 e−04	9, 58	1.57 e−03
12% CrO_3/Al_2O_3	Acidic	59	6.42 e−03
5% CrO_3/TiO_2	2.46 e−02	59	3.41 e−03
$Fe_2(MoO_4)_3$	2.12 e−02	18	2.55 e−03
18% MoO_3/Al_2O_3	6.29 e−03	18	1.52 e−03
6% MoO_3/TiO_2	2.83 e−02	18	8.04 e−03
17% Re_2O_7/Al_2O_3	Acidic	60	6.60 e−03
5% Re_2O_7/TiO_2	9.86 e−02	60	4.48 e−03

[a] The IR data have been extrapolated to 45.6 Torr (Langmuir kinetic model, Eq. [17], using metal site density parameters from Table 3) and the fixed-bed data were taken from the indicated references. Note that the TOFs for the supported vanadia catalysts are not exactly the same as in (9) due to averaging with data from other references. Also, some literature data were adjusted for temperature using published activation energies (TOF values being generally constant with metal oxide coverage (4)).

adsorption isotherm in the kinetic model. Specifically, Table 3 indicates that the TOF for 3% V_2O_5/CeO_2 is somewhat lower than that of 5% V_2O_5/TiO_2, which is the opposite behavior as that observed in traditional fixed-bed reactors (9, 21). However, Table 3 also indicates that the vanadia/ceria catalyst has a lower Langmuir adsorption constant, K_{ads}, and a higher surface decomposition constant, k_{rds}, than the vanadia/titania catalyst. Since the surface decomposition rate constant, k_{rds}, is only a function of temperature, the effect of increasing methanol partial pressure will be focused on increasing the steady-state concentration of the methoxylated intermediates, θ_m, as shown in Fig. 10A. The vanadia/titania catalyst experiences a smaller change in θ_m due its already high adsorption at 1.52 Torr, so at the higher methanol pressure (45.6 Torr) the vanadia/ceria catalyst is able to approach a θ_m similar to that of the vanadia/titania catalyst. This finally translates into a higher TOF for vanadia/ceria compared to vanadia/titania at 45.6 Torr, as shown in Fig. 10B and Table 4, because the surface decomposition rate has not changed with increasing pressure. A linear adsorption model would not have predicted this behavior.

Similar extrapolations of the IR-cell catalytic data to 45.6 Torr methanol were done for the other catalysts and are presented in Table 4 with the TOF values from PFR studies also listed for comparison. For consistency with the PFR data, total surface active metal site densities were used in these extrapolations of the IR-cell data, despite their previously described deficiencies. It is interesting to note that the relative differences in TOF between different catalysts are largely the same for both techniques and indicate that the IR-cell catalytic data is most likely self-consistent. Moreover, the TOF variations between the two techniques are generally within an order of magnitude for a given catalyst (sometimes better), which is rather good agreement considering the dramatically different experimental setups.

To assess the mechanistic origin of the ligand effect in metal oxide catalysts, the kinetic parameters for supported

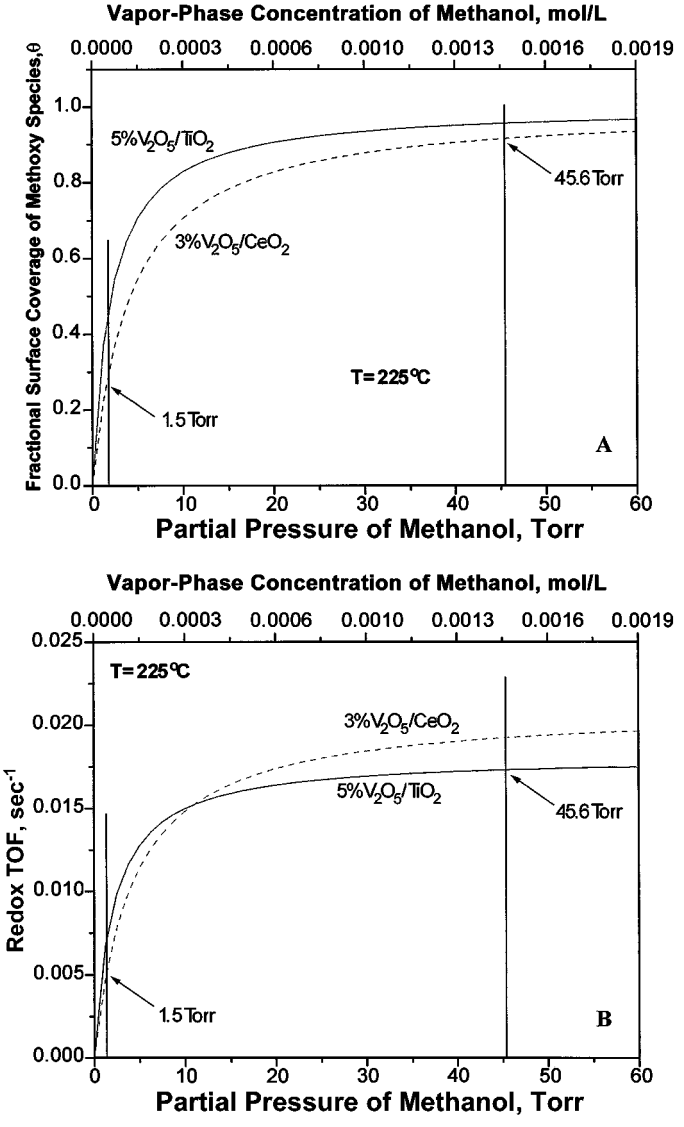

FIG. 10. (A) Predicted fractional surface coverages of methoxylated surface intermediates on vanadia/titania and vanadia/ceria monolayer catalysts at 225°C, as a function of methanol partial pressure. Curves were determined using the full Langmuir isotherm (Eq. [16a]) and the parameter values calculated in Table 3 (chemisorption site densities). (B) Predicted TOFs of vanadia/titania and vanadia/ceria monolayer catalysts at 225°C, as a function of methanol partial pressure. Curves were determined using the full Langmuir kinetic model (Eq. [17]) and the parameter values calculated in Table 3 (chemisorption site densities).

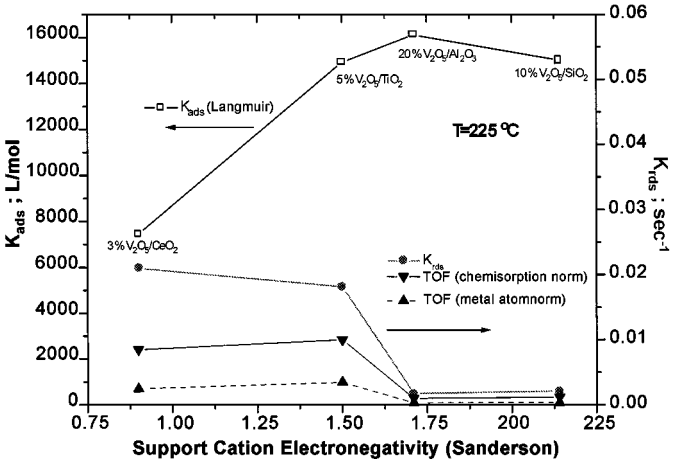

FIG. 11. Comparison of kinetic parameters at 225°C for supported vanadia monolayer catalysts as a function of ligand (support) cation electronegativity. The equilibrium adsorption constant, K_{ads}, is scaled to the left axis (units of L/mol), while the TOFs and surface decomposition rate constant, k_{rds}, are scaled to the right axis (both quantities with units of s^{-1}).

vanadia catalysts, as calculated in Table 3 using the full Langmuir model, have been plotted as a function of ligand (support) cation electronegativity in Fig. 11. Several conclusions may be drawn from this figure. First, redefining TOF based on methanol chemisorption data increases the TOF values by a factor of about three but otherwise does not alter the trend with ligand electronegativity. This is related to the similar vanadia site densities that are observed across all of the supported vanadia catalysts (42), which, in turn, are three times higher than the (also similar) methanol chemisorption site densities (18). More significantly, the TOF clearly correlates with the rate constant for the surface decomposition step, k_{rds}, which varies by a factor of ∼12 across the different supported vanadia catalysts. By contrast, the adsorption constant, K_{ads}, is relatively invariant at $\sim 1.5 \times 10^4$ L/mol for vanadia supported on alumina, titania, and silica, decreasing in value by about half only for the vanadia/ceria catalyst. Similar trends in K_{ads} and k_{rds} are observed for supported molybdena catalysts in Table 3. The trends in supported chromia and rhenia catalysts, which have been generally less studied than supported vanadia and molybdena systems, are more scattered and will require further investigation.

The parameter values for the supported vanadia catalysts also compare relatively favorably with those obtained in the previously cited IR/mass spectrometer flow study (21). However, the magnitudes of variation in the previous study (∼22-fold for k_{rds} and ∼6-fold for K_{ads}) are somewhat exaggerated because the IR extinction coefficient for the adsorbed methoxylated surface species was only measured on the vanadia/titania catalyst and assumed to be the same on the other systems. Subsequent work showed that the extinction coefficients are moderately different as the support is changed, even though the methoxylated surface species are all still adsorbed onto vanadia monolayers (18). The present investigation used individual extinction coefficients for each catalyst (as determined in (18)) to improve the analysis.

Overall, the presently observed mechanistic behavior of supported vanadia and molybdena catalysts confirms the previously documented (9, 21) correlation between overall TOF and ligand cation electronegativity, the more electropositive ligands (titania and ceria support cations) always having higher TOFs than the more electronegative ligands (alumina and silica support cations). More fundamentally, the electronegativity of the ligand cation determines the magnitude of the rate-determining decomposition of surface methoxylated intermediates, k_{rds}, which is believed to occur via the hydride abstraction of a methyl hydrogen by the active metal cation. Quantum mechanical calculations have suggested that this hydride abstraction process is strongly dependent on the density of accessible electronic states in the support cation, thereby providing a possible theoretical explanation of the ligand effect (56). The adsorption step, represented by an equilibrium adsorption constant, K_{ads}, is generally much less sensitive to the ligand cation electronegativity and has a less significant (but still important) impact on overall TOF. This may indicate that methanol adsorption on supported metal oxides is largely localized on the active metal cation (V, Mo, etc.), so that the support influence is felt mainly during the hydride abstraction step described previously.

5. CONCLUSIONS

The mechanistic origin of the ligand effect on the methanol oxidation TOFs to formaldehyde in metal oxide catalysts was investigated in the present study using a novel *in situ* IR cell designed to operate as a fixed-bed catalytic reactor. An online GC analysis was used to obtain gas-phase product distributions. The catalytic results indicate that the cell is actually working as a differential reactor ($E_{app} \sim 15$–18 kcal/mol) for the majority of catalysts studied (vanadia/silica being the exception with a mass transfer limited E_{app} of less than 10 kcal/mol). Quantification of the adsorbed, steady-state concentrations of methoxylated surface intermediates by *in situ* IR spectroscopy allowed for decoupling of the reaction mechanism and kinetics to yield individual estimates of the adsorption equilibrium constants for the methanol adsorption step and the kinetic rate constants for the rate-determining surface decomposition step.

These calculations indicate that site densities determined from methanol chemisorption experiments are preferable to total active metal atom site densities, the latter being of greater magnitude, because the metal-based site densities

do not account for the higher *fractional* surface coverages that actually exist during real catalytic conditions. Furthermore, the kinetic expressions applicable to low-moisture, highly methoxylated surface coverage conditions were developed and found to require the use of the full Langmuir isotherm based on the relatively high fractional surface coverages of methoxylated intermediates measured during the experiments. Lastly, comparisons of the relative values of the adsorption equilibrium constants, K_{ads}, and the kinetic rate constants for the surface decomposition step, k_{rds}, indicate that the TOF clearly correlates with the rate constant for the surface decomposition step. For example, supported vanadia catalysts exhibit a 12-fold increase in the surface decomposition rate constant, k_{rds}, for vanadia supported on silica, alumina, titania, and ceria supports. Conversely, the adsorption constant, K_{ads}, is relatively invariant for vanadia supported on silica, alumina, and titania, decreasing in value by about half only for the vanadia/ceria catalyst.

It appears that the fundamental origin of the ligand effect on the overall TOF is most likely related to the electronegativity of the ligand cation, the more electropositive ligands (titania and ceria support cations) always having higher TOFs than the more electronegative ligands (alumina and silica support cations). The electronegativity of the ligand cation determines the magnitude of the rate-determining decomposition of surface methoxylated intermediates, k_{rds}, via its influence on the hydride abstraction of methyl hydrogen by the active metal cation. The adsorption step, represented by an equilibrium adsorption constant, K_{ads}, is generally much less sensitive to the ligand cation electronegativity and has a less significant (but still important) impact on overall TOF. In fact, it is likely that methanol adsorption on supported metal oxides is largely localized on the active metal cation (V, Mo, etc.), so that the support influence is felt mainly during the hydride abstraction step.

APPENDIX: ARRHENIUS EQUATIONS

The following equations were used to calculate the kinetic parameters given in Table 3 (see Ref. 21 and references therein for more theoretical details about these equations). The calculations begin by first determining K_{ads} and k_{rds} at each measured temperature, using Eq. [17] in conjunction with the measured catalytic TOFs (from GC analysis) and the surface concentrations of methoxylated intermediates (from IR). Next, the logarithms of the Arrhenius equations given below (Eqs. [A1] and [A2]) are used to generate the slopes and intercepts of the general plot: ln(left-hand side) vs $1/T$. The slopes and intercepts then yield the desired parameters, including A_{ads}, ΔH, A, and E_a. The entropies of transition, $\Delta S^{\ddagger}$, are simply calculated algebraically at a given temperature of 498 K (225°C), using the calculated values for A at that temperature.

Adsorption equilibrium constant for methoxylated surface intermediates

$$K_{ads} = A_{ads} \exp(+|\Delta H|/RT). \quad [A1]$$

Kinetic rate constant for surface decomposition of methoxylated surface species

$$k_{rds} = A \exp(-E_a/RT). \quad [A2]$$

Entropies of transition

$$A = (kT/h) \exp(\Delta S^{\ddagger}/R), \quad [A3]$$

where k is the Boltzmann constant, h is the Planck constant, and R is the gas constant.

ACKNOWLEDGMENT

The authors gratefully acknowledge the United States Department of Energy–Basic Energy Sciences (Grant DEFG02-93ER14350) for financial support of this work.

REFERENCES

1. (a) Thomas, J. M., and Thomas, W. J., "Principles and Practice of Heterogeneous Catalysis." VCH Publishers, New York, 1997. (b) Special issue of *Topics in Catalysis*, "Catalyst Characterization Under Reaction Conditions" (J. M. Thomas and G. A. Somorjai, Eds.), Vol. 8, No. 1–2, 1999.
2. Gerberich, H. R., and Seaman, G. C., *in* "Kirk-Othmer Encyclopedia of Chemical Technology," 4th ed., Vol. 11, p. 929. Wiley, New York, 1994.
3. Tatibouët, J. M., *Appl. Catal. A* **148**, 213 (1997).
4. Wachs, I. E., Deo, G., Vuurman, M. A., Hu, H., Kim, D. S., and Jehng, J. M., *J. Mol. Catal.* **82**, 443 (1993).
5. Roozeboom, F., Cordingley, P. D., and Gellings, P. J., *J. Catal.* **68**, 464 (1981).
6. Forzatti, P., Tronconi, E., Elmi, A. S., and Busca, G., *Appl. Catal. A*. **157**, 387 (1997).
7. Deo, G., and Wachs, I. E., *J. Catal.* **146**, 323 (1994).
8. Wachs, I. E., Deo, G., Jehng, J. M., Kim, D. S., and Hu, H., *in* "Heterogeneous Hydrocarbon Oxidation," ACS Symposium Series 638 (B. K. Warren and S. T. Oyama, Eds.), p. 292. ACS Press, Washington, DC, 1996.
9. (a) Wachs, I. E., Deo, G., Juskelis, M. V., and Weckhuysen, B. M., *in* "Dynamics of Surfaces and Reaction Kinetics in Heterogeneous Catalysis" (G. F. Froment and K. C. Waugh, Eds.), p. 305. Elsevier, Amsterdam, 1997. (b) Wachs, I. E., *in* "Catalysis" (J. J. Spivey, Ed.), Vol. 13, p. 37. The Royal Society of Chemistry, Cambridge, 1997. (c) Gao, X., Bare, S. R., Fierro, J. L. G., and Wachs, I. E., *J. Phys. Chem. B* **103**, 618 (1999).
10. Hu, H., and Wachs, I. E., *J. Phys. Chem.* **99**, 10911 (1995).
11. Kim, D. S., Wachs, I. E., and Segawa, K., *J. Catal.* **146**, 268 (1994).
12. Busca, G., *J. Mol. Catal.* **50**, 241 (1989).
13. Elmi, A., Tronconi, E., Cristiana, C., Martin, J. G., Forzatti, P., and Busca, G., *Ind. Eng. Chem. Res.* **28**, 387 (1989).
14. Busca, G., Elmi, A., and Forzatti, P., *J. Phys. Chem.* **91**, 5263 (1987).
15. Niwa, M., Sano, M., Yamada, H., and Murakami, Y., *J. Catal.* **151**, 285 (1995).
16. Yamada, H., Niwa, M., and Murakami, Y., *Appl. Catal. A* **96**, 113 (1993).

17. Matsuoka, Y., Niwa, M., and Murakami, Y., *J. Phys. Chem*. **94**, 1477 (1990).
18. (a) Burcham, L. J., Ph.D. dissertation, Chapter 4, Lehigh University, Bethlehem, PA, 2000. (b) Burcham, L. J., Briand, L. E., and Wachs, I. E., *Langmuir*, in press (2001).
19. Arena, F., Frusteri, F., and Parmaliana, A., *Appl. Catal. A* **176**, 189 (1999).
20. Khodakov, A., Olthof, B., Bell, A. T., and Iglesia, E., *J. Catal.* **181**, 205 (1999).
21. Burcham, L. J., and Wachs, I. E., *Catal. Today* **49**, 467 (1999).
22. Special issue of *Catal. Today* **9** (1991).
23. Topsoe, N.-Y., *Science* **265**, 1217 (1994).
24. Matyshak, V. A., and Krylov, O. V., *Catal. Today* **25**, 1 (1995).
25. Kaul, D. J., and Wolf, E. E., *J. Catal.* **93**, 321 (1985).
26. Kaul, D. J., and Wolf, E. E., *J. Catal.* **89**, 348 (1984).
27. Venter, J. J., and Vannice, M. A., *Appl. Spectrosc.* **42**, 1096 (1988).
28. Arakawa, H., Fukushima, T., and Ichikawa, M., *Appl. Spectrosc.* **40**, 884 (1986).
29. Vannice, M. A., Moon, S. H., Twu, C. C., and Wang, S.-Y., *J. Phys. E: Sci. Instrum*. **12**, 849 (1979).
30. Saladin, F., Meier, A., and Kamber, I., *Rev. Sci. Instrum*. **67**, 2406 (1996).
31. Li, B., and Gonzalez, R. D., *Appl. Spectrosc.* **52**, 1488 (1998).
32. Penninger, J. M. L., *J. Catal.* **56**, 287 (1979).
33. Szilagyi, T., Koranyi, T. I., Paal, Z., and Tilgner, J., *Catal. Lett.* **2**, 287 (1989).
34. Komiyama, M., and Obi, Y., *Rev. Sci. Instrum*. **67**, 1590 (1996).
35. Tinker, H. B., and Morris, D. E., *Rev. Sci. Instrum*. **43**, 1024 (1972).
36. Friedman, R. M., and Dannhardt, H. C., *Rev. Sci. Instrum*. **56**, 1589 (1985).
37. Igarashi, A., Ogino, Y., and Onodera, S., *Rev. Sci. Instrum*. **44**, 321 (1973).
38. Bell, A. T., *in* "Vibrational Spectroscopy of Molecules on Surfaces" (J. T. Yates and T. E. Madey, Eds.), p. 105. Plenum, New York, 1987.
39. Moser, W. R., Cnossen, J. E., Wang, A. W., and Krouse, S. A., *J. Catal.* **95**, 21 (1985).
40. Gotz, R., Mizaikoff, B., and Kellner, R., *Appl. Spectrosc.* **52**, 1248 (1998).
41. Xiao, H., Dai, S., Young, J. P., Feigerle, C. S., and Edwards, A. G., *Appl. Spectrosc.* **52**, 626 (1998).
42. Wachs, I. E., *Catal. Today* **27**, 437 (1996).
43. Briand, L., Gambaro, L., and Thomas, H., *J. Catal.* **161**, 839 (1996).
44. Burcham, L. J., and Wachs, I. E., *Spectrochim. Acta, Part A* **54**, 1355 (1998).
45. Gao, X., Bare, S. R., Weckhuysen, B. M., and Wachs, I. E., *J. Phys. Chem. B* **102**, 10842 (1998).
46. Lavalley, J. C., *Catal. Today* **27**, 377 (1996).
47. Lavalley, J. C., and Sheppard, N., *Spectrochim. Acta* **28A**, 2091 (1972).
48. Busca, G., *Catal. Today* **27**, 457 (1996).
49. Nakamoto, K., "Infrared and Raman Spectra of Inorganic and Coordination Compounds" 4th ed. Wiley, New York, 1986.
50. Bailes, M., and Stone, F. S., *Catal. Today* **10**, 303 (1991).
51. Suda, Y., and Morimoto, T., *Langmuir* **3**, 786 (1987).
52. Knozinger, H., Kochloefl, K., and Meye, W., *J. Catal.* **28**, 69 (1973).
53. Farneth, W. E., Ohuchi, F., Staley, R. H., Chowdhry, U., and Sleight, A. W., *J. Phys. Chem*. **89**, 2493 (1985).
54. Zhang, W., Oyama, S. T., and Holstein, W. L., *Catal. Lett.* **39**, 67 (1996).
55. Holstein, W. L., and Machiels, C. J., *J. Catal.* **162**, 118 (1996).
56. Weber, R. S., *J. Phys. Chem*. **98**, 2999 (1994).
57. Gao, X., and Wachs, I. E., unpublished results, 1999.
58. Jehng, J.-M., *J. Phys. Chem. B* **102**, 5816 (1998).
59. Kim, D. S., and Wachs, I. E., *J. Catal.* **142**, 166 (1993).
60. Kim, D. S., and Wachs, I. E., *J. Catal.* **141**, 419 (1993).